Fluid-structure interaction modeling on a three-dimensional ray-strengthened caudal fin

Guangyu Shi[1], Qing Xiao[1,a)], Qiang Zhu[2] and Wei Liao[3]

[1]*Department of Naval Architecture, Ocean and Marine Engineering, University of Strathclyde, Glasgow,*

G4 0LZ, Scotland, UK

[2]*Department of Structural Engineering, University of California San Diego, La Jolla, California, 92093,*

USA

[3]*Bihrle Applied Research Inc., Hampton, VA 23666, USA*

In this paper, we present a numerical model capable of solving the fluid-structure interaction problems involved in the dynamics of skeleton-reinforced fish fins. In this model, the fluid dynamics is simulated by solving the Navier-Stokes equations using a finite-volume method based on an overset, multi-block structured grid system. The bony rays embedded in the fin are modeled as nonlinear Euler-Bernoulli beams. To demonstrate the capability of this model, we numerically investigate the effect of various ray stiffness distributions on the deformation and propulsion performance of a three-dimensional caudal fin. Our numerical results show that with specific ray stiffness distributions, certain caudal fin deformation patterns observed in real fish (e.g., the cupping deformation) can be reproduced through passive structural deformations. Among the four different stiffness distributions (uniform, cupping, W-shape and heterocercal) considered here, we find that the cupping distribution requires the least power expenditure. The uniform distribution, on the other hand, performs the best in terms of thrust generation and efficiency. The uniform stiffness distribution, *per se*, also leads to 'cupping' deformation patterns with relatively smaller phase differences between various rays. The present model paves the way for future work on dynamics of skeleton-reinforced membranes.

_____

a) Author to whom correspondence should be addressed. Electronic mail: qing.xiao@strath.ac.uk.Tel: +44 01415484779.

1. Introduction

Ray-finned fish distinguish themselves from other aquatic animals by the composite design of their fins featuring soft membranes supported by bony rays [1]. These fins are important not only for steady locomotion, but also for maneuvering, motion stabilizing and sensing, during which a fish can adjust the fin shape and orientation to vector the hydrodynamic forces [2]. In terms of morphology, fish fins fall into two categories: paired fins (pectoral fin and pelvic fin) and median fins (dorsal fin, anal fin and caudal fin). By coordinating the movements of different fins, ray-finned fish exhibit a great variety of locomotion modes, among which the fin-activated swimming style attracts increasing interests from scientists and engineers as it provides a promising prototype for biomimetic propellers. Indeed, fin-activated swimming mode requires little body deformation and thus greatly simplifies the mechanical design [3].

Due to the important role it plays in locomotion, caudal fin has been extensively studied both experimentally [4]–[11] and numerically [12]–[17] over the past decades. Traditionally, it is either considered as an extension of the fish body or modeled as a rigid or elastic flapping foil. By using uniform materials and two DOF motions (e.g. heave and pitch), the simplification may severely compromise the evaluation efficiency, maneuverability and controllability of the system. In fact the caudal fin of bony fish has complicated internal structure [1], [18], allowing it to perform multiple DOF motions that can generate locomotion forces in the lateral, vertical and forward directions [19], [20]. Structurally, a caudal fin is composed of a soft and thin collagenous membrane supported by bony fin rays. The Young's modulus of the collagenous membrane is much smaller than that of the embedded rays, thus the bending stiffness of the caudal fin is mainly determined by those rays. The non-uniform bending stiffness of each ray and the differences among the stiffness of different rays lead to anisotropic structural properties. Apart from this feature, these fins also possess two other characters associated with the multi-degree-of-freedom control over the fin surface. The first one is the sophisticated musculature system attached to the rays. These muscles can work independently, enabling individual actuation of each ray. The second character is the unique bio-mechanical design of the fin rays themselves. According to previous morphological studies [20], [21], a fin ray has a bi-laminar structure and embedded tendons. By pulling the tendons, a fish can actively change the curvature and bending stiffness of each ray.

2

Owing to the capability in force generation, fish fins attract much attention from researchers in biology, engineering, and other related fields. New experimental techniques allow them to conduct live fish experiments to visualize and reconstruct the fin movements, the surrounding flow field, and the muscle activities [22] [20], [23]–[27]. Based on these studies it was concluded that the dynamics of fish fins are essentially three dimensional with multiple DOF. For example, the caudal fin of the bluegill sunfish (*Lepomis macrochirus*) possesses morphological symmetry, but it functions asymmetrically with a larger lateral excursion at the dorsal lobe [23]. Besides, the bluegill sunfish can modulate the caudal fin shapes (e.g., cupping and 'S'-shape) to achieve various maneuvering behaviors [27]. Although experiments using live fish shed light on the kinematics and hydrodynamics of fins, the disadvantages and limitations of this approach are also obvious [8]. Primarily, it is impossible to study the effect of individual traits on the performance. Another limitation is the lack of sufficient diversity among extant species. To address these issues, an alternative method is to construct fin-like robotic devices [28]–[31]. This approach allows more freedom in alternating the parameters (e.g., geometry, material properties, and kinematics) so that the effect of each parameter can be isolated [22]. Park et al. [28] experimentally examined a biomimetic caudal fin with various shapes and bending stiffness to identify the optimal kinematic condition maximizing the thrust generation. They concluded that the maximum thrust was achieved when the phase difference between the driving motion and the passive bending motion was close to 90 degrees. Nevertheless, the fin in their experiment was constructed with uniform material, which is very different from the ray-strengthened caudal fin considered in the present paper. Esposito et al. [30] designed a more complicated robotic caudal fin based on bluegill sunfish. With six individually controlled and activated flexible fin rays, this mechanical caudal fin can reproduce both symmetrical and asymmetrical deformation patterns observed in experiments. Among these motions, the cupping motion was found to generate the largest mean thrust in most cases. Larger thrust was obtained with stiffer fin rays and higher flapping frequency. It was also demonstrated that the difference between various motion patterns was most pronounced at lower motion frequency and higher ray flexibility. Besides, their results also indicate that there are different optimal ray stiffnesses under different scenarios such as motion program, flapping frequency and Reynolds number.

From the perspective of underwater robotics design, it would be beneficial if we could explore a large parameter space to find the optimal combination. However, neither studies on live fish nor those using mechanical devices allow this. For example, the bending stiffness of the caudal fin plays a crucial role on its performance, however, we do not know if the caudal fins of live fish are at the optimal flexibility.

3

Although mechanical devices can be constructed with different structural properties, they are still subjected to the availability of materials. These restrictions can be circumvented in computational modeling. Moreover, numerical simulations can provide holographic information of the flow field as well as physical insight of the fluid-structure interactions. The advantage of examining "what if" type of questions makes the computational modeling more appealing compared with experiments [32]. With the advancement of high-performance computers and high-fidelity numerical algorithms, computational modeling has become an indispensable complement to experimental studies [32], [33]. With sophisticated computational fluid dynamics (CFD) tools, some researchers have numerically analyzed the hydrodynamics of a highly deformable fish fin [34], [35] and the fin-body/fin-fin interactions [36], [37]. In these simulations, the motions of the fish fins are prescribed based on experimentally recorded data. However, as mentioned above, the fin rays are highly flexible and can be actively controlled, thus strong fluid-structure interactions are involved in fish locomotion. To address this, Zhu and Shoele [38] developed a fully coupled fluid-structure interaction model to investigate the performance of a ray-strengthened caudal fin, where the fin rays were represented as nonlinear beams with uniform elasticity and the flow around the caudal fin was assumed to be inviscid and resolved with a boundary-element method. By individually controlling the rotation of each ray at the basal end, the caudal fin can accomplish both homocercal (symmetrical dorsal-ventral motion) and heterocercal (asymmetrical dorsal-ventral motion) modes. In both cases, they found that flexibility can greatly enhance the thrust generation by introducing an effective pitch motion and improve the propulsion efficiency due to the reduction of lateral force. Besides, passive deformation also reduces the sensitivity of propulsive performance to the kinematics of the fin. With the same model, they also examined the propulsion performance of skeleton-reinforced pectoral fins in labriform swimming [39], [40]. However, the flows involved in fish locomotion are often dominated by boundary-layer separations and vortex-based mechanics, which are a direct effect of viscosity. Although the inviscid models are computationally inexpensive and allow a quick evaluation of the key flow features over a large parameter space, the inherent weaknesses of these models may lead to inaccurate results. Yet, relatively little work has been done in using Navier-Stokes solvers to study the fluid-structure interactions of ray-supported fins. Shoele and Zhu numerically examined the propulsive performance of skeleton supported pectoral fins [41] and insect wings [42] with a Navier-Stokes model. They concluded that the non-uniform stiffness distribution may significantly improve the performance, especially with a strengthened leading edge. However, their simulations are all two-dimensional.

4

Bearing this in mind, in this paper we developed a fully coupled fluid-structure interaction model to examine the propulsive performance of a ray-supported caudal fin which is structurally similar to the caudal fin of a real fish. In this model, the fluid dynamics around the caudal fin is simulated by solving the Navier-Stokes equations with a finite-volume method, while the fin rays are modeled as nonlinear Euler-Bernoulli beams. The rays are actuated by imposing a sway motion at the basal ends and the rest part of the rays is deformed passively under its own inertia, the elastic effect, the hydrodynamic load and the constraint from the elastic membrane. It should be noted that in the present paper we use a ray-strengthened caudal fin to demonstrate the capability of our code; however, the code itself can be used in a wide range of applications. There are two purposes of the present work: first, to elucidate the effects of various spanwise deformation patterns on the propulsion performance of a ray-strengthened caudal fin. A similar problem was numerically studied with a boundary-element method for the fluid dynamics [43], where the leading edge vortices and vortices shed from the dorsal and ventral edges as well as the viscous shear stresses were not considered. These effects may have substantial influence on the performance of the caudal fin. Second, it serves as the framework for future research involving various fin configurations as well as active controlling.

The present work will be the first systematic fully-viscous fluid-structure investigation of a fin-like propeller that captures a key morphologic characteristic of the ray fins of bony fish, the anisotropic distribution of bending stiffness imparted by the composite architecture with an underlying soft membrane with embedded rays. Compared with potential-flow-based simulations based on boundary-integral formations [43], this model includes not only viscous friction on the solid surface but also vorticity shedding from locations other than the trailing edge (e.g. the side edges), which is expected to affect the dynamics of the system significantly. Moreover, the development of this fluid-structure interaction method will be a critical step towards more sophisticated modeling of fish fins including active shape change through individual ray control.

The rest of this paper is organized as follows: in section 2, the geometrical and structural properties as well as the kinematics of the idealized caudal fin are described. The parameters characterizing the propulsion performance are also defined in this section. In the next section, we introduce the governing equations and the numerical methods used in the present paper. In section 4, several validation cases and sensitivity studies are demonstrated. The numerical results, including the forces, efficiencies and wake

5

signature of caudal fins with various distributions of ray stiffness are presented in section 5. The conclusions are drawn in the final section.

2. Problem Statement

In the present study, an idealized three-dimensional fin (as shown in Figure 1 (a)) is numerically examined. The fin is modeled as a rectangular membrane supported by evenly distributed rays. The lengths in both x- and z-directions are c, resulting in an aspect ratio of unity. The thickness is selected to be $h=0.004c$. Kinematically, the front end (i.e. the basal end) of each ray undergoes a sinusoidal sway motion in y-direction, which is depicted as $y(t) = y_0 cos(2\pi f t)$, where y_0 is the sway amplitude and f is the motion frequency. In the present simulations, we select $y_0=0.5c$ and the Strouhal number is defined as $S_t = \frac{2fy0}{U_\infty}$. It should be noted that this definition of the Strouhal number is different from the one based on the tip excursion. This is because the displacement of the trailing edge varies along the span so that it is difficult to specify a tip excursion.

The fin considered here has 11 evenly distributed rays (typical number in a real fish fin varies from 10 to 20, [29]) with various bending stiffness. Each ray is structurally represented by a nonlinear beam with uniform Young's modulus. The normalized bending stiffness of the ith ray is defined as $K_i = \frac{E_i I}{\rho U_\infty^2 c^3}$ ($i=1,…,N$), where $N = 11$, E_i is the Young's modulus of the ray and ρ is the fluid density. In this study, we assume that the bending stiffness of the membrane itself is negligible, i.e., the rigidity of the fin is solely determined by the stiffness of the rays. However, the membrane does provide constraints upon the ray's motion, which are modeled as linear springs. Based on our numerical tests, the spring constant here is chosen to be $0.02\rho U_\infty c$, i.e., the springs are soft enough to allow large spanwise deformations, yet stiff enough to prevent too much expansion of the membrane. To reduplicate various fin deformations observed in previous experiments [30] and simulations [43], four different distributions of K_i, which correspond to four different deformation patterns, are considered in the present work:

1) Uniform distribution: $K_i = K_b$.

2) Cupping distribution: $K_i = K_b Q_i/Q$, where $Q_i = 1 + \lambda \left[1 - sin\left(\frac{\pi(i-1)}{N-1}\right)\right]$.

3) W-shape distribution: $K_i = K_b Q_i/Q$, where $Q_i = 1 + \lambda \left[1 - \left|sin\left(\frac{2\pi(i-1)}{N-1}\right)\right|\right]$.

4) Heterocercal distribution: $K_i = K_b Q_i/Q$, where $Q_i = 1 + \lambda \left[1 - sin\left(\frac{\pi(i-1)}{2(N-1)}\right)\right]$.

6

Here K_b is a constant and measures the mean stiffness of all the rays and $Q = \frac{1}{N}\sum_{i=1}^{N} Q_i$. The parameter λ is selected to be 1, i.e., the stiffness of the least flexible ray is twice that of the most flexible one. Apart from the bending stiffness, another important parameter for this problem is the mass ratio, which is defined as $m^* \equiv \rho_s h/\rho c$, where h is the thickness of the fin. Here the mass ratio is selected to be m^*=0.2.

The propulsion performance of the fin is characterized by the mean thrust coefficient $\overline{C_T}$, the mean power expenditure coefficient $\overline{C_P}$ and the propulsion efficiency η. Here $\overline{C_T}$ is calculated by averaging the instantaneous thrust coefficient $C_T(t)$ over one motion period T. The thrust coefficient is defined as

$$C_T(t) = \frac{-F_X(t)}{1/2\,\rho U_\infty^2 c^2},$$
(1)

where $F_X(t)$ is the x-component of the instantaneous hydrodynamic force $\mathbf{F}(t)$.

Similarly, we have

$$C_P(t) = \frac{P(t)}{1/2\,\rho U_\infty^3 c^2},$$
(2)

where $P(t)$ is the instantaneous power expenditure, which is evaluated as

$$P(t) = \iint_S \mathbf{F}(\mathbf{x}, t) \cdot \mathbf{V}_g(\mathbf{x}, t)d\mathbf{x},$$
(3)

where $\mathbf{V}_g(\mathbf{x}, t)$ is the moving velocity of the fin. The mean power expenditure coefficient $\overline{C_P}$ is then calculated by averaging power coefficient $C_P(t)$ over one motion period. We assume that the energy transferred from the fluid to the caudal fin cannot be reused, thus the negative values of $C_P(t)$ are set to be zero. Therefore, the propulsion efficiency η is calculated as

$$\eta = \frac{\overline{C_T}}{\overline{C_P}}$$
(4)

It is worthy to point out that we are not exactly duplicating the real fish caudal fin geometrically and materially. Instead, we extract some key features (ray-strengthened, anisotropic flexibility and fluid-structure interaction) possessed by real fish caudal fin, aiming at providing some useful guidelines for bio-inspired robotic fin design. Additionally, the present work is definitely not a simple repeat of Zhu and Bi [43]. Instead, we use a more sophisticate flow solver which is physically more accurate (e.g. the

7

capturing of vorticity shedding from the leading, dorsal, and ventral edges). The present work also paves the way for future research involving active control over the curvature and stiffness of the fin rays.

3. Mathematical Formulations and Numerical Methods

The flow solver and its coupling with a modal analysis method have been extensively validated in our previous studies [44]–[47]. In our recent work, the flow solver is coupled with a nonlinear beam model [48]. We further developed a fully coupled fluid-structure interaction solver based on overset grids to simulate the aforementioned three-dimensional ray-supported caudal fin model shown in Figure 1 (a). The present FSI code consists of five main modules: a finite-volume based computational fluid dynamics (CFD) solver, a nonlinear beam model, an overset grid assembler, a mesh deformation algorithm and a fluid-structure coupling procedure.

3.1 The CFD solver

The fluid solver numerically solves the unsteady Navier-Stokes equations, which can be expressed in the integral form as

$$\frac{\partial}{\partial t} \iiint_{\Omega} \boldsymbol{U} dV + \iint_{\partial \Omega} \boldsymbol{G} d\boldsymbol{S} = 0, \tag{5}$$

where Ω is the control volume, $\partial\Omega$ is the boundary surface enclosing the volume, and $\boldsymbol{S}$ is the surface vector in outward direction. In Equation (5), the conservative variable vector $\boldsymbol{U}$ is defined as

$$\boldsymbol{U} = (\rho, \rho\boldsymbol{v}, \rho E)^T, \tag{6}$$

where ρ is the fluid density, $\boldsymbol{v}$ is the velocity vector in Cartesian coordinate system, and E is the total energy. The flux vector $\boldsymbol{G}$ (which consists of a convective term and a diffusive term) can be formulated as

$$\boldsymbol{G} = \begin{bmatrix} \rho\widetilde{\boldsymbol{v}}^T \\ \rho\widetilde{\boldsymbol{v}}\boldsymbol{v} + p\boldsymbol{I} \\ (\rho E\widetilde{\boldsymbol{v}} + p\boldsymbol{v})^T \end{bmatrix} + \begin{bmatrix} 0 \\ \boldsymbol{\tau} \\ (\boldsymbol{\tau} \cdot \boldsymbol{v} - \boldsymbol{q})^T \end{bmatrix}, \tag{7}$$

where $\widetilde{\boldsymbol{v}}$ is the relative velocity calculated as $\widetilde{\boldsymbol{v}} = \boldsymbol{v} - \boldsymbol{v}_g$, and $\boldsymbol{v}_g$ the grid velocity. The shear stress $\boldsymbol{\tau}$ and heat flux $\boldsymbol{q}$ in Equation (7) are defined as

$$\boldsymbol{\tau}_{\alpha\beta} = \mu\left[\left(\frac{\partial v_{\alpha}}{\partial x_{\beta}} + \frac{\partial v_{\beta}}{\partial x_{\alpha}}\right) - \frac{2}{3}(\nabla \cdot \boldsymbol{v})\delta_{\alpha\beta}\right], \\ \boldsymbol{q} = -\kappa\nabla T \tag{8}$$

8

where $\alpha, \beta \in (x, y, z)$, μ and κ are the dynamic viscosity and the thermal conductivity respectively, and T is the temperature.

Based on an overset, multi-block structured grid system [49], the fluid governing equations are discretized by a cell-centred finite volume method. For each hexahedral cell (i, j, k), we have the following semi-discrete form:

$$\frac{\partial}{\partial t}\left(U_{i,j,k}\Delta\Omega_{i,j,k}\right) - R_{i,j,k} - D_{i,j,k} = 0, \tag{9}$$

where $R_{i,j,k}$ measures the convective and diffusive fluxes entering the hexahedral cell through its surface. $D_{i,j,k}$ denotes the artificial viscosity that is used to stabilize the scheme and eliminate the spurious numerical oscillations [50].

For unsteady simulations, the dual-time stepping algorithm [51] is employed for the temporal integration, where Equation (9) is reformulated as a steady-state problem with a pseudo-time $\tilde{t}$:

$$\frac{\partial}{\partial\tilde{t}}U^{n+1} = \frac{1}{\Delta\Omega^{n+1}}\widetilde{R}(U^{n+1}), \tag{10}$$

where

$$\widetilde{R}(U^{n+1}) = R(U^{n+1}) + D(U^{n+1}) - \frac{3(U\Delta\Omega)^{n+1} - 4(U\Delta\Omega)^n + (U\Delta\Omega)^{n-1}}{2\Delta t}. \tag{11}$$

Equation (10) is then integrated by a hybrid multistage Runge-Kutta scheme. The flow solver is finally parallelized to reduce the computational time via Message Passing Interface (MPI). More detailed formulations including the boundary conditions can be found in Ref. [52].

It is worth noting that the present CFD code solves the compressible Navier-Stokes equations without turbulent models, i.e., the flow is assumed to be laminar. When the Reynolds number is relatively low (e.g. below 10^3), turbulence may have insignificant effects on the flow field. For these scenarios, a laminar flow model is usually adopted to study some biomimetic problems, see examples in Ref. [32], [35], [36], [41]. To simulate incompressible flows with a compressible flow solver, it is necessary to ensure that the compressibility effect is negligibly small. A flow can be considered as incompressible if the Mach number (defined as $M_a = U/a$, where U and a are the flow velocity and speed of sound respectively) is below the critical value of 0.3. In the current paper, we choose the freestream Mach number to be $M_{a,\infty} = 0.06$, which is far below the critical value but still sufficiently large for numerical

9

stability. Considering the problems with moving boundaries, the actual Mach number experienced by the body can be larger than $M_{a,\infty}$. To ensure the accuracy of the present flow solver, the local Mach numbers in the whole computational domain are monitored to guarantee that it is below the critical value. The present CFD code has been successfully applied to investigate various incompressible flow problems in our previous publications [44]–[48].

3.2 Nonlinear beam model

Structurally, the fin rays are modeled as nonlinear Euler-Bernoulli beams with uniform bending stiffness, whose dynamics is governed by [53]

$$m_s \frac{\partial^2 \boldsymbol{x}}{\partial t^2} + K_b \frac{\partial^4 \boldsymbol{x}}{\partial s^4} - K_h \frac{\partial}{\partial s} \left\{ \left[1 - \left(\frac{\partial \boldsymbol{x}}{\partial s} \cdot \frac{\partial \boldsymbol{x}}{\partial s} \right)^{-1/2} \right] \frac{\partial \boldsymbol{x}}{\partial s} \right\} = \boldsymbol{F}_f + \boldsymbol{F}_e, \tag{12}$$

where $\boldsymbol{x}$ is the instantaneous position of the ray, and s ($0 < s < c$) is the Lagrangian coordinate. $m_s = \rho_s h$ is the mass per unit length, where ρ_s is the structural density and h is the thickness of the fin, $K_b = Eh^3/12$ and $K_h = Eh$ represent the bending and stretching stiffness respectively. $\boldsymbol{F}_f$ denotes the fluid loads and $\boldsymbol{F}_e$ represents the external forces from connecting linear springs which model the constraints from the collagenous membrane. The hysteretic (or material) damping effect is considered by replacing the Young's modulus E in K_b and K_h with $E(1 + \sigma \partial/\partial t)$, where σ denotes the structural damping coefficient. In all present simulations, we select $\sigma = 2c/U_\infty$.

At the front end ($s = 0$) of each ray, the boundary condition with prescribed motion is imposed, we have

$$\begin{aligned} \boldsymbol{x}(0, t) &= \boldsymbol{x}(0,0) + [0, y(t)]^T \\ \frac{\partial \boldsymbol{x}(0, t)}{\partial s} &= [1,0]^T \end{aligned}. \tag{13}$$

At the trailing end, we have the free boundary condition (zero-stress and zero-bending) which can be mathematically expressed as

$$\begin{aligned} K_b \frac{\partial^3 \boldsymbol{x}}{\partial s^3} - K_h \left[1 - \left(\frac{\partial \boldsymbol{x}}{\partial s} \cdot \frac{\partial \boldsymbol{x}}{\partial s} \right)^{-1/2} \right] \frac{\partial \boldsymbol{x}}{\partial s} &= 0 \\ \frac{\partial^2 \boldsymbol{x}}{\partial s^2} &= 0 \end{aligned}. \tag{14}$$

Equation (12), together with boundary conditions (13) and (14), are both spatially and temporally discretized using a second-order finite difference method and the resulting linear system is solved with an iterative Gauss-Seidel approach [14], [53].

10

3.3 Overset grid assembler

The present overset grid assembler (OGA) is based on the implicit hole cutting (IHC) technique [54], which requires no explicit definition of the hole boundary. The IHC method is combined with the multi-block structured grid system by introducing the concept of 'cluster' [49]. A cluster is a grid composed of one or multiple blocks with matched boundaries between them. For example, Figure 2 (a) demonstrates the overset, multi-bock structured grid used for CFD simulations of the present caudal fin. This overset grid system consists of two clusters: one is the background grid (green colour), which provides a sufficient far-field boundary. Another cluster is the body-fitted grid around the body (red colour), which is denser than the background mesh and is mainly used to capture the fluid features near the body. In the present overset grid method, block boundaries are classified into three categories: the physical boundary, matching boundary and overlapping boundary. At the physical boundary, physical boundary conditions (e.g., inlet, outlet, no-slip etc.) are applied. The matching boundary is the boundary where blocks are connected exactly in a point-to-point fashion. This boundary only exists between blocks in the same cluster and the fluid information is exchanged through two-layer of ghost cells around each block. The overlapping boundary is the non-physical outer boundary of one cluster, where the flow information is interpolated from the corresponding donors using a trilinear scheme. To ensure accurate data transfer between different clusters, the two layers of ghost cells are also included as fringe cells and join the grid connectivity.

The IHC method is intrinsically a process of selecting the optimal 'donor' for each 'receiver' based on the criterion of cell size. The donor cell for a receiver point in one cluster refers to the cell on another cluster containing the receiver point, as illustrated in Figure 2 (b). For a given receiver point Q, a key task of the IHC approach is to find its optimal donor cell. The donor detection algorithm implemented in the present work consists of three basic steps: 1) *Low-order inside/outside cell test*. The test uses a quick cross and dot product calculation to check if the testing point (receiver) is inside or outside a cell (potential donor). 2) *High-order inside/outside cell test*. This test is triggered after a potential donor is identified using the low-order test, which requires the computational coordinate (ξ) of the testing point within this cell. 3) *Cell size based donor selection*. If multiple donor cells are found after previous two steps, the one with the smallest cell volume will be selected as the optimal donor cell.

The donor searching process (also known as hole-cutting process) is particularly time consuming, thus special efforts are made in two aspects to reduce the cost. First, the overlapping boundary points are

11

tested prior to interior points in order to eliminate unnecessary tests. During the searching for donor cells for the boundary points, the overlapping relationship between different blocks will be determined. When testing the interior points, the IHC algorithm will skip those blocks that are non-overlapping with the testing block, which tremendously reduces the computational cost. Second, the starting cell for a donor search in a particular block is carefully selected to shorten the searching path. In most cases, the present and the previous test points are in close proximity, which indicates that the donor cells of the two test points are also very close to each other. By carefully choosing the starting cell, the search path can be considerably shortened [54]. The basic steps of the present overset grid algorithm are therefore designed as:

1) Separating the complete geometry into different components.

2) Generating a multi-block structured grid for each component, and assembling them into a single overset grid.

3) Testing the overlapping boundary points including the ghost-cell points and establishing the overlapping relationship between different blocks.

3) Testing the interior points. Non-overlapping blocks are skipped in this process.

4) Organizing and distributing the donor information to the other processors to facilitate the parallel computation.

After the aforementioned hole cutting procedure, all grid cells in the overset grid system are categorized into calculated cell and interpolated cell. If a cell fails to find the corresponding donor cell, it will be labelled as calculated cell; otherwise, it is known as interpolated cell. The fluid variables of the calculated cells will be updated normally while the values of these variables of the interpolated cells need to be obtained from their corresponding donor cells. Overset grids have great advantages in handling bodies with complex geometries and multiple bodies with relative motion. Despite that only a single caudal fin model is used in the present study, the use of overset grids enables the present work to be easily extended to problems involving fin-fin and/or fin-body interactions.

3.4 Mesh deformation algorithm

Due to the use of overset grids, only grids associated with a flexible body need to be deformed. In the present work, the mesh deformation is determined using a fast and robust moving mesh algorithm [55]. This approach combines a spring-analogy method [56] and a trans-finite interpolation (TFI) method. Specifically, the corner points of a mesh block are assumed to be connected via linear springs, whose

12

rigidity is inversely proportional to its length. Given the new positions of the corners on the deformed surface, the positions of the other corner points will be decided by solving the static equilibrium equations. After the positions of all corner points are calculated, the coordinates of the block inner points are interpolated via TFI method.

3.5 Fluid-structure coupling procedure

In the present code, the Navier-Stokes solver is coupled with the nonlinear beam model via a partitioned framework. In partitioned method, a strong coupling can be achieved by introducing subiterations within each time step [57] [58], which has second-order time accuracy and allows lager time step. However, with full subiterations, the computational cost can be substantially increased, which offsets the benefit of larger time step. Alternatively, a loosely coupled method referred as Conventional Serial Staggered (CSS) procedure [59] can also be accomplished within the partitioned framework. This method requires only one data exchange between the fluid solver and structural solver in each time step so that it significantly reduces the computational expense. Despite the numerical stability issue associated with loosely coupled methods, this approach is still favoured due to its simplicity and efficiency. Since the caudal fin model is completely three-dimensional and requires plenty of computational time, the loosely coupled CSS approach is used in the present work, as illustrated in Figure 3 (a).

Since the fluid and structural equations are solved independently, the structural grid does not necessarily coincide with the body-fitted fluid grid (shown in Figure 3 (b)). Thus, interpolations of fluid forces and structural deformations must be performed between the two grid systems. Figure 3 (c) shows the method used to transfer the fluid loads from the fluid grid to the structural grid. Both the fluid mesh vertices on the wet boundary of the body and the structural grid points are firstly projected to a common planar plane, on which a linear (bilinear for two-dimensional case) interpolation is then performed. The structural displacements are transferred to the fluid mesh by a constant volume tetrahedron (CVT) method [60][61]. As shown in Figure 3 (d), the tetrahedron is composed of three points in structural grid plus one point from fluid grid. When the structural points are moved to new positions, the fluid point is moved such that the volume of the tetrahedron remains unchanged.

4. Validations and Self-consistency Study

The present FSI solver based on multi-block grid has been validated and used to investigate the dynamics of a three-dimensional caudal fin slice in our previous work [48]. In the current paper, an

13

overset grid module is integrated into the FSI code, which extends the capability of the present code dealing with multiple flexible bodies. To further validate the present FSI solver with the overset grid function, we simulate three canonical problems and compare our results with those from theory or other literature. The first case is used to validate the present three-dimensional flow solver, where the flow past a 3D plunging wing is simulated. To examine the accuracy of the structural model, the first and second order bending modes of a cantilever are produced by heaving the beam with very small amplitude at its first and second natural frequencies respectively. The coupled FSI solver is then validated by predicting the dynamic response of a flexible cantilever immersed in the wake of a square cylinder. Additionally, a self-consistency study is also conducted to check the sensitivities of the present code to CFD mesh density and physical time step size.

4.1 Validation cases

We first simulate the flow past a three-dimensional cylinder and compare the present results with those from the literature [62], [63]. The Reynolds number based on freestream velocity U_∞ and diameter D is 300. Two different aspect ratios ($L/D = 6.28$ and 10.24) are used, consistent with those in the literature. Figure 4 illustrates the temporal evolutions of lift and drag coefficients and the iso-surfaces of normalized vorticity magnitude at these two aspect ratios. It can be seen that for both cases, the time histories of force coefficients show a modulated behavior. A similar phenomenon is observed in Ref. [63]. We can also observe from Figure 4 (c) and (d) that the vortex shedding behind the 3D cylinder is completely three-dimensional. The mean value of drag coefficient and the root-mean-square (r.m.s.) value of lift coefficient from the present simulation and the literature are summarized in Table 1. It can be seen that the present results agree well with the published data.

To examine the accuracy of the present structural solver, we numerically reproduce the first and second order bending modes of a cantilever by imposing a heave motion with small amplitude at the leading edge of the beam. The parameters are chosen as follows: length l=0.1 m, thickness h=0.001 m, density ρ_s=10 kg/m^3, Young's modulus E=100 GPa, and heave amplitude a_0=0.5h. The natural frequencies of a cantilever can be calculated as

$$\omega_i = \left(\frac{\beta_i}{l}\right)^2 \sqrt{\frac{EI}{\rho_s S}} \ (i = 1, 2, \cdots), \tag{15}$$

where I is second moment of inertia, S is the cross-section area, and , β_i=1.875 and 4.694 for the first and second order natural frequencies respectively. The modal functions are expressed as

14

$$\phi_i(x) = cos(\beta_i x) - ch(\beta_i x) + \zeta_i[sin(\beta_i x) - sh(\beta_i x)] \ (i = 1, 2, \cdots), \tag{16}$$

where

$$\zeta_i = -\frac{cos(\beta_i l) + ch(\beta_i l)}{sin(\beta_i l) + sh(\beta_i l)} \ (i = 1, 2, \cdots). \tag{17}$$

The first two bending mode shapes are shown in Figure 5. It can be observed that the calculated and theoretical results agree perfectly well with each other.

Finally, we numerically predict the dynamics of a thin elastic cantilever placed in the wake of a stationary rigid square cylinder (as shown in Figure 6 (a)) in order to validate the coupled algorithm. This case has been widely used as validation benchmark for fluid-structure interaction solvers [58], [64]–[66]. When the Reynolds number is higher than a critical value, the flow separates from the leading corners of cylinder at a constant frequency. The oscillating flow results in the oscillation of lifting force, which excites the flexible cantilever attached behind it to vibrate accordingly. The dimensionless parameters for the fluid and structure are as follows: The structure to fluid mass ratio m^*=1.27, the bending stiffness of the cantilever K_b=0.226 and the Reynolds number based on the diameter of the square cylinder is 332. The overset grid used for fluid dynamics simulation is shown in Figure 6 (b), where independent clusters are generated for the square body and the cantilever.

The time history of the dimensionless cantilever tip displacement is demonstrated in Figure 6 (c), from which we can see that the vibration of the cantilever becomes periodic after a transient region. Figure 6 (d) shows vorticity contours when the beam reaches the extreme positions. It is observed that flow separates at the leading corners and a clockwise vortex forms at the upper region while its counterpart forms at the lower region. These vortices travel along the vibrating cantilever and dissipate into the wake. The vortices at the trailing edge shed into the wake forming the famous Von Karman vortex street. The quantitative reduced frequency ($f_r = \pi f D/U_\infty$) and the dimensionless maximal tip displacement (d_{max}^*) are summarized in Table 2 along with other available data. Obviously, present results agree well with others from the literature though the reduced frequency in the present simulation is slightly higher than the results from referred literatures [58], [64]–[66]. The maximal tip displacement obtained here d_{max}^*=1.12 is close to those using different FSI solvers, which ranges from1.02 to 1.25.

4.2 Self-consistency study

15

In order to check the dependency of the current numerical results on the CFD mesh density and physical time step size, simulations are carried out for cupping stiffness distribution at K_b=1.0 and S_t=0.4. Since the near fluid field around the caudal fin has more significant effect on the fin's performance, only the mesh density of Cluster 2 (see Figure 2) is varied in mesh dependency test and the background mesh (Cluster 1) remains unchanged. The computational domain of the body-fitted cluster is essentially a box. The mesh density is changed via adjusting the number of grid point along three directions. A fine mesh (MESH_F) is generated with 201×161×81 grid points in x-, y-, and z-direction respectively. Similarly, a medium mesh (MESH_M) and a coarse mesh (MESH_C) are generated with 161×141×61 grid points and 121×121×41 grid points respectively. Figure 7 (a) shows the instantaneous thrust coefficient within one motion period using different body-fitted meshes. It is observed that the thrust produced by the three meshes perfectly agree with each other, indicating that MESH_M is sufficient to simulate the three-dimensional caudal fin case. With MESH_M, we then examine the sensitivity of the present CFD code to the physical time step size using three different time steps. The results are illustrated in Figure 7 (b), from which we find that dt=T/200 is sufficient to simulate the flow field around the caudal fin. Therefore, in the following simulations, we use MESH_M and dt=T/200 to investigate the proposed problem.

5. Results

The three-dimensional caudal fin problem depicted in Figure 1 is solved using the aforementioned fluid-structure interaction solver in Section 3. Figure 8 shows the computational domain for fluid dynamics. The origin is located at the leading edge of Ray 1 and the flow direction is along the x-axis. On the fin surface, we apply the no-slip boundary condition; while for the other boundaries, the non-reflective far-field boundary condition is imposed. The Reynolds number, which governs the fluid behavior, is defined as $Re = \frac{\rho U_\infty c}{\mu}$, where μ is the fluid dynamic viscosity, and in the present simulations we choose Re=1000.

Figure 9 demonstrates the fin deformations within one motion period for various stiffness distributions. From the top views, we can see that the deformation patterns from different stiffness distributions are quite similar to each other, with the bending of all the fin rays dominated by the lowest mode. However, for the deformation patterns viewed from behind, different stiffness distributions demonstrate distinctive features. Despite the fact that all the rays are identical, the fin with uniform stiffness distribution also displays spanwise deformation (Figure 9 (b)), which resembles a cupping deformation. This can be attributed to the non-uniformly distributed fluid forces along the span of the fin due to the finite aspect

16

ratio and the vortices rolling up at the dorsal and ventral edges (Ray 11 and Ray 1 respectively). For the cupping distribution of the ray stiffness (Figure 9 (d)), the rays at the dorsal and ventral edges lead the sway motion while the ray in the middle (Ray 6) falls behind. This is because the ray in the middle is softer than those at the upper and lower edges, and the hydrodynamic loading on the central part of the fin is larger than elsewhere. With the W-shape stiffness distribution, the fin deformations become more complicated, where multiple curvature reversals are generated. The heterocercal stiffness distribution generates asymmetrical deformation patterns, which distinguishes itself from the other stiffness distributions, where the deformations obtained are symmetrical with respect to the center line (Ray 6). It should be noted that the fin deformation patterns in the present paper are achieved solely by passive ray deflections. In the experiments of Esposito et al. [30], the fin deformations were modulated by changing the phases and excursions of the fin rays, which are intrinsically different from the approach we use here.

Figure 10 shows the mean thrust coefficient $\overline{C_T}$, the mean power expenditure coefficient $\overline{C_P}$ and the propulsion efficiency η as functions of the mean bending stiffness of the rays for different distributions at S_t=0.4. The rigid ray case is also included for comparison. From these figures, we can see that the rigid fin cannot generate any net thrust at this Strouhal number, as the longitudinal force is mostly provided by shear stresses due to the lack of effective pitching motion. This is different from the result of Zhu and Bi [43], where finite thrust was generated by a rigid caudal fin. The difference is attributed to the fact that the fin used in our study is much thinner than the one used by Zhu and Bi (0.004c vs. 0.02c) so that the component of the pressure force in the forward direction is significantly reduced. Moreover, the current model includes viscous friction on the fin surface, which further diminishes the thrust. Within the range of bending stiffness considered here, all flexible fins have improved propulsion performance with increased thrust and efficiency. For all types of stiffness distributions, the mean thrust coefficient $\overline{C_T}$ experiences a significant increase and then a sharp decline with the increase of the flexibility, with the peak $\overline{C_T}$ values achieved at an optimal flexibility of K_b=1.0 [11]. A similar trend is seen in the propulsion efficiency, where the peaks are achieved at smaller K_b values, which vary with specific stiffness distribution profiles. Interestingly, a slight increase of the power expenditure $\overline{C_P}$ is witnessed at stiffer rays for all types of stiffness distributions. But due to the fact that $\overline{C_T}$ is increased at a larger magnitude, the efficiency still rises. As the bending stiffness becomes smaller than the optimal value, both the thrust coefficient $\overline{C_T}$ and the power expenditure coefficient $\overline{C_P}$ begin to fall, but $\overline{C_P}$ drops with a larger rate, resulting in an increase of the propulsion efficiency. As the mean stiffness K_b further decreases, $\overline{C_T}$ decreases faster than $\overline{C_P}$, which causes a significant decline in efficiency.

17

A closer inspection of Figure 10 reveals that when the mean bending stiffness K_b is larger than the optimal flexibility value, the differences between various stiffness distributions are marginal. The thrust forces generated by cupping and W-shape distributions are only slightly higher than those from uniform and heterocercal distributions. However, the differences become more pronounced when the fins are more flexible, which is consistent with previous simulations [43] while contradictory with the experimental study [30], where they concluded that with more compliant fin rays, the forces generated by the robotic caudal fin are less varied. However, we note that there exists fundamental difference in terms of the mechanism used to actuate the rays and create various deformation patterns between the present work and the experiment. In our cases, all fin rays undergo the same sway motion at the basal ends and the various deformations are accomplished passively. On contrary, in the experiment, the robotic rays were activated individually, and various fin shapes were created by varying the phase lags between different rays. Generally, more flexible fin rays are more compliant to surrounding flows. For the present simulations, compliance enlarges the differences between the deflections of fin rays, thus magnifying the effect of various stiffness distributions. In the experiment, the compliance of the robotic fin rays mitigates the effects of phase lags between them and reduces the differences between various deformation patterns.

As aforementioned, in the present study, softer caudal fins have more distinctive deformation patterns under different bending stiffness distributions. Therefore, the differences in thrust generation and efficiency between various stiffness distributions are more pronounced for fins with more flexibility, which can be observed in Figure 10. Specifically, for very soft caudal fins, the uniform distribution creates the largest thrust and highest propulsion efficiency, whereas the cupping distribution generates the least thrust and lowest efficiency. But cupping distribution has the lowest power expenditure coefficient. The W-shape and the heterocercal distributions only have mediocre performance. Figure 11 shows the same plots as Figure 10 at a smaller Strouhal number (S_t=0.3), from which we can draw the same conclusions.

The present conclusion that the fin with uniform stiffness distribution has the best overall performance in terms of thrust generation and efficiency seems to be different with those from previous experimental [30] and numerical [43] studies. For example, Esposito et al. [30] found that the cupping motion produced more thrust than the other motions (flat, W, undulation and rolling). However, as previously

18

mentioned, the mechanism to actuate the fin rays in the numerical studies is different from the one in experiments. Besides, we should note that the uniform distribution in the present work does not correspond to the flat motion in the experiment. In the present paper, the uniform stiffness distribution eventually results in cupping deformation patterns due to the non-uniform distribution of the fluid loads along the fin span, which will be shown later. This cupping effect is more pronounced in softer rays. From this perspective, our conclusion is actually consistent with the experiment. Zhu and Bi [43] numerically examined a similar problem, where they concluded that the 'W'-shape distribution performed the best, which is also different from the present simulation. The difference is likely to be attributed to the methods used to resolve the surrounding flows: an inviscid flow model was used by Zhu and Bi, which neglected the viscous effect and vortices shed from the leading edge and the dorsal and ventral edges. These vortices are believed to significantly affect the pressure distribution across the fin surface, thereby affecting the performance [67].

The instantaneous thrust coefficient, lateral force coefficient and power expenditure coefficient within one flapping period for both rigid and flexible fins are shown in Figure 12. The most pronounced effect of the structural flexibility is the significant increase in the peak value of C_T. This is attributed to larger flapping amplitude and effective pitching angle due to the structural deformation, which will be discussed later. Another effect of flexibility is the reduction in lateral force C_Y. This can be explained by the fact that flexibility can significantly reduce the work done to the surrounding fluid so that less energy is needed to activate the caudal fin.

The lateral deflection of the caudal fin rays essentially creates a pitch motion, which can be expressed as $(y_T - y_L)/c$, where y_T and y_L are the lateral displacement of the ray's trailing edge and leading edge respectively. Figure 13 demonstrates the lateral deflections of the leading edge, trailing edge and pitch motion of Ray 6, together with the thrust coefficient C_T in cupping distribution at two different values of K_b. The amplitude of the ray's trailing edge is larger than that of the leading edge due to the lateral deflection, which leads to a stronger wake and thereby enhancing the thrust generation. Another factor contributing to higher thrust is the creation of a pitch motion, which redirects the fluid forces acting on the fin surface and generates larger component in forward direction. Comparing the pitch motion curve (green dash-dot-dot line) with the C_T curve (pink solid line), we can observe that the peak value of the thrust is accomplished at the largest relative displacement (corresponding to the largest pitch angle). A closer observation and comparison of Figure 13 (a) and (b) reveal that the thrust generation is also

19

greatly affected by the phase lag between the lateral motion and the pitch motion. For example, at K_b=1.0, where the largest mean thrust coefficient is achieved (see Figure 10), the phase lag between the lateral motion and the pitch motion is approximately 76 degrees while the phase lag at K_b=0.3, where the lowest thrust is generated, is found to be around 105 degrees, which is considered out of the optimal range [28]. We note that the phase lag maximizing the thrust generation in our study deviates from the optimal value obtained experimentally by Park et al. [28]. This may be attributed that the mechanical caudal fins used by Park et al. have uniform material properties; whilst in the present study, the bending stiffness is varied along the span, leading to more complicated deformation patterns. Another reason may be the effect of mass ratio. To enhance numerical stability, the mass ratio is chosen to be 0.2 in the present simulations, whereas the mass ratio used in the experiment of Park et al. is below 0.03.

The actual lateral deflections of Ray 1 and Ray 6 for two different stiffness distributions within one flapping period are shown in Figure 14. Overall, the deformation patterns from uniform and cupping distributions are similar to each other, indicating that the uniform distribution actually leads to a cupping deformation. However, for the cupping distribution, Ray 6 deforms much more significantly due to the lower bending stiffness while Ray 1 has smaller lateral deflection, which creates a higher phase lag between the two rays.

The wake behind the flexible caudal fin is demonstrated in Figure 15. As we can see that for all stiffness distributions, the wake is composed of a sequence of vortex-rings that are comparable with the caudal fin in size. For the symmetrical deformations with respect to the center line (uniform, cupping and W-shape), the vortex rings behind the fin are also symmetrical and resemble each other. Only subtle difference at the connection between neighboring rings can be observed. However, for the asymmetrical deformation (heterocercal), it is evident that the vortex-rings are tilted upward compared with those from symmetrical deformations. The force component in vertical direction is thus significantly increased, which can be used for maneuvering and stabilizing. A sectional view of the wake behind the caudal fin is shown in Figure 16. With symmetrical stiffness distributions, the fin produces a pair of tip vortices from the trailing edges of the dorsal (Ray 11) and ventral (Ray 1) rays. These vortices are countering-rotating and have approximately equal strength. For the fin with heterocercal stiffness distribution, there are also two counter-rotating tip vortices (with different strength) shed from the ray trailing edges.

6. Discussions and Conclusions

20

With active and passive control over the bony rays embedded in the collagenous membrane, ray-finned fish are able to modulate their caudal fin shapes to obtain desired forces in different directions. This unique composite architecture of the caudal fin has three main features: 1) anisotropic flexibility over the fin; 2) individual activation of the rays; 3) control on the ray's curvature and stiffness. These features enable the fish to have multi-degree-of-freedom control over their caudal fins, and also provide a source of inspiration for the design of bio-inspired underwater robotics. However, the complicated structure of fish fin poses great challenges for computational modeling. With a few exceptions, most numerical studies idealize fish caudal fins as either rigid or elastic panels with uniform flexibility. These oversimplified models are believed to produce inaccurate conclusions.

In this paper, we develop a fully coupled fluid-structure interaction model that can be used to study skeleton-strengthened fish fins. In this model, the fluid dynamics is resolved by an in-house CFD code, where the unsteady Navier-Stokes equations are solved by a finite-volume method based on an overset, multi-block structured grid system. The embedded rays are represented by nonlinear Euler-Bernoulli beams. The membranes connecting different rays are assumed to be unable to hold any bending, thus their constraints on the rays are modeled as linear springs.

To demonstrate the capability of the present model and elucidate the effects of various spanwise deformation patterns on the propulsion performance of fish fins, we numerically examine a three-dimensional ray-supported caudal fin. With four spanwise stiffness distributions (uniform, cupping, W-shape and heterocercal), certain deformation patterns observed in experiments can be reproduced. For all stiffness distributions, the performance of the caudal fin is enhanced over a wide range of flexibility. Both the thrust and the efficiency experience an increase and then a decrease as the flexibility rises, indicating the existence of an optimal flexibility. The differences between various stiffness distributions are more pronounced in softer rays. Among these stiffness distributions, uniform distribution is found to have the best overall performance in terms of thrust generation and efficiency, while the cupping distribution requires the least power expenditure. This conclusion seems to contradict previous experimental study [30]. By analyzing the actual deformations, however, it is found that with a uniform bending stiffness distribution, the caudal fin produces a 'cupping' deformation as well due to the non-uniformly distributed fluid loads across the fin surface. Subsequently, both uniform and cupping stiffness distributions lead to cupping deformation patterns. But the cupping distribution is more likely to be "over-cupped" (i.e. the passive ray deformations are out of phase with the swaying motions),

21

which explains why the thrust generated by the cupping distribution drops much more significantly than that by the uniform distribution.

The current model is concentrated on illustrating the effect of ray stiffness distribution on the hydrodynamic performance of fish-like fins with passive deformation, whereas some details of actual fish fins (e.g. the geometry) are not considered. For example, for simplicity in this model the rays are assumed to have the same length. This, together with the inclusion of viscous effect and more sophisticated vorticity shedding model, may explain the differences in the current results and those in the previous study (Ref. 43). The fins of live fish, on the other hand, rely on both passive and active control for fin shape variation. It is thus difficult to directly relate predictions from the current model with dynamics of actual fish fins.

The present study suggests that by appropriately cupping their fins, fish are able to save energy and generate more desired forces when moving against incoming surrounding fluids. This conclusion is consistent with previous observations [24], [26], [30]. On the other hand, unlike the fully passive fin dynamics depicted in our model, fish can actively control the curvature and flexibility of their fins, which is expected to further enhance the locomotion performance. These effects will be examined in future studies.

Acknowledgements

Reference

[1]   G. V Lauder and E. G. Drucker, "Morphology and Experimental Hydrodynamics of Fish Fin Control Surfaces," *IEEE J. Ocean. Eng.*, vol. 29, no. 3, pp. 556–571, 2004.

[2]   E. G. Drucker and G. V. Lauder, "Function of pectoral fins in rainbow trout: behavioral repertoire and hydrodynamic forces," *J. Exp. Biol.*, vol. 206, pp. 813–826, 2003.

[3]   A. Raj and A. Thakur, "Fish-inspired robots: design, sensing, actuation, and autonomy—a review of research," *Bioinspiration and Biomimetics*, vol. 11, no. 3, 2016.

[4]   M. S. Triantafyllou, A. H. Techet, and F. S. Hover, "Review of experimental work in biomimetic foils," *IEEE J. Ocean. Eng.*, vol. 29, no. 3, pp. 585–594, 2004.

[5]   G. S. Triantafyllou, M. S. Triantafyllou, and M. A. Grosenbaugh, "OPTIMAL THRUST DEVELOPMENT IN OSCILLATING FOILS WITH APPLICATION TO FISH PROPULSION," *J. Fluids Struct.*, vol. 7, p. 205, 1993.

[6]   J. M. Anderson, K. Streitlien, D. S. Barrett, and M. S. Triantafyllou, "Oscillating foils of high propulsive efficiency," *J. Fluid Mech.*, vol. 360, pp. 41–72, 1998.

[7]   D. A. Read, F. S. Hover, and M. S. Triantafyllou, "Forces on oscillating foils for propulsion and maneuvering," *J. Fluids Struct.*, vol. 17, no. 1, pp. 163–183, 2003.

[8]   G. V. Lauder, B. Flammang, and S. Alben, "Passive robotic models of propulsion by the bodies and caudal fins of fish," *Integr. Comp. Biol.*, vol. 52, no. 5, pp. 576–587, 2012.

[9]   L. Wen and G. Lauder, "Understanding undulatory locomotion in fishes using an inertia-compensated flapping foil robotic device," *Bioinspiration and Biomimetics*, vol. 8, no. 4, 2013.

[10]   K. N. Lucas, P. J. M. Thornycroft, B. J. Gemmell, S. P. Colin, J. H. Costello, and G. V Lauder, "Effects of non-uniform stiffness on the swimming performance of a passively- fl exing , fi sh-like foil model," *Bioinspir. Biomim.*, vol. 10, no. 5, 2015.

[11]   A. K. Kancharala and M. K. Philen, "Optimal chordwise stiffness profiles of self-propelled flapping fins," *Bioinspiration and Biomimetics*, vol. 11, no. 5, 2016.

[12]   I. H. Tuncer and M. F. Platzer, "Thrust generation due to airfoil flapping," *AIAA J.*, vol. 34, no. 2, pp. 324–331, 1996.

[13]   G. C. Lewin and H. Haj-Hariri, "Modelling thrust generation of a two-dimensional heaving airfoil in a viscous flow," *J. Fluid Mech.*, vol. 492, no. 492, pp. 339–362, 2003.

[14]   Q. Zhu, "Numerical simulation of a flapping foil with chordwise or spanwise flexibility," *AIAA J.*, vol. 45, no. 10, pp. 2448–2457, 2007.

[15]   H. Dai, H. Luo, P. J. S. A. F. de Sousa, and J. F. Doyle, "Thrust performance of a flexible low-aspect-ratio pitching plate," *Phys. Fluids*, vol. 24, no. 10, pp. 1–9, 2012.

[16]   R.-N. Hua, L. Zhu, and X.-Y. Lu, "Locomotion of a flapping flexible plate," *Phys. Fluids*, vol. 25, no. 25, pp. 121901–111902, 2013.

[17]   P. D. Yeh and A. Alexeev, "Free swimming of an elastic plate plunging at low Reynolds number," *Phys. Fluids*, vol. 26, no. 5, 2014.

[18]   G. V. Lauder, "Caudal Fin Locomotion in Ray-Finned Fishes Historical and Functional Analyses," *Am. Zool.*, vol. 29, pp. 85–102, 1989.

[19]   G. V. Lauder and P. G. A. Madden, "Learning from Fish: Kinematics and Experimental Hydrodynamics for Roboticists," *Int. J. Autom. Comput.*, vol. 4, pp. 325–335, 2006.

[20] G. V. Lauder and P. G. A. Madden, "Fish locomotion: Kinematics and hydrodynamics of flexible foil-like fins," *Exp. Fluids*, vol. 43, no. 5, pp. 641–653, 2007.

[21] S. Alben, P. G. Madden, and G. V Lauder, "The mechanics of active fin-shape control in ray-finned fishes.," *J. R. Soc. Interface*, vol. 4, no. 13, pp. 243–56, 2007.

[22] G. V. Lauder, "Fish Locomotion: Recent Advances and New Directions," *Ann. Rev. Mar. Sci.*, vol. 7, no. 1, pp. 521–545, 2015.

[23] G. V. Lauder, "Function of the Caudal Fin during Locomotion in Fishes Kinematics Flow Visualization and Evolutionary Patterns," *Am. Zool.*, vol. 29, pp. 101–122, 2000.

[24] E. D. Tytell, "Median fin function in bluegill sunfish Lepomis macrochirus: streamwise vortex structure during steady swimming," *J. Exp. Biol.*, vol. 209, pp. 1516–1534, 2006.

[25] E. D. Tytell, E. M. Standen, and G. V. Lauder, "Escaping Flatland: three-dimensional kinematics and hydrodynamics of median fins in fishes," *J. Exp. Biol.*, vol. 211, no. 2, pp. 187–195, 2008.

[26] B. E. Flammang and G. V Lauder, "Speed-dependent intrinsic caudal fin muscle recruitment during steady swimming in bluegill sunfish, lepomis macrochirus," *J. Exp. Biol.*, vol. 211, no. Pt 4, p. 587, 2008.

[27] B. E. Flammang and G. V Lauder, "Caudal fin shape modulation and control during acceleration, braking and backing maneuvers in bluegill sunfish, Lepomis macrochirus.," *J. Exp. Biol.*, vol. 212, no. Pt 2, p. 277, 2009.

[28] Y. J. Park, U. Jeong, J. Lee, S. R. Kwon, H. Y. Kim, and K. J. Cho, "Kinematic condition for maximizing the thrust of a Robotic Fish using a compliant caudal fin," *IEEE Trans. Robot.*, vol. 28, no. 6, pp. 1216–1227, 2012.

[29] K. L. Feilich and G. V. Lauder, "Passive mechanical models of fish caudal fins: Effects of shape and stiffness on self-propulsion," *Bioinspiration and Biomimetics*, vol. 10, no. 3, p. 36002, 2015.

[30] C. J. Esposito, J. L. Tangorra, B. E. Flammang, and G. V. Lauder, "A robotic fish caudal fin: effects of stiffness and motor program on locomotor performance," *J. Exp. Biol.*, vol. 215, no. 1, pp. 56–67, 2012.

[31] Z. Ren, X. Yang, T. Wang, and L. Wen, "Hydrodynamics of a robotic fish tail: Effects of the caudal peduncle, fin ray motions and the flow speed," *Bioinspiration and Biomimetics*, vol. 11, no. 1, 2016.

[32] R. Mittal, H. Dong, M. Bozkurttas, G. V. Lauder, and P. Madden, "Locomotion with flexible propulsors: II. Computational modeling of pectoral fin swimming in sunfish," *Bioinspiration and Biomimetics*, vol. 1, no. 4, 2006.

[33] R. Mittal, "Computational modeling in biohydrodynamics: Trends, challenges, and recent advances," *IEEE J. Ocean. Eng.*, vol. 29, no. 3, pp. 595–604, 2004.

[34] M. Bozkurttas, H. Dong, R. Mittal, P. Madden, and G. Lauder, "Hydrodynamic Performance of Deformable Fish Fins and Flapping Foils," *44th AIAA Aerosp. Sci. Meet. Exhib.*, no. January, pp. 1–11, 2006.

[35] H. Dong, M. Bozkurttas, R. Mittal, P. Madden, and G. V. Lauder, "Computational modelling and analysis of the hydrodynamics of a highly deformable fish pectoral fin," *J. Fluid Mech.*, vol. 645, pp. 345–373, 2010.

[36] G. Liu, Y. Ren, H. Dong, O. Akanyeti, J. C. Liao, and G. V. Lauder, "Computational analysis of vortex dynamics and performance enhancement due to body-fin and fin-fin interactions in fish-like locomotion," *J. Fluid Mech.*, vol. 829, pp. 65–88, 2017.

[37] R. Li *et al.*, "A multi-body dynamics based numerical modelling tool for solving aquatic biomimetic problems," *Bioinspiration and Biomimetics*, vol. 13, no. 5, 2018.

[38] Q. Zhu and K. Shoele, "Propulsion performance of a skeleton-strengthened fin.," *J. Exp. Biol.*, vol. 211, pp. 2087–2100, 2008.

[39] K. Shoele and Q. Zhu, "Fluid-structure interactions of skeleton-reinforced fins: performance analysis of a paired fin in lift-based propulsion.," *J. Exp. Biol.*, vol. 212, pp. 2679–2690, 2009.

[40] K. Shoele and Q. Zhu, "Numerical simulation of a pectoral fin during labriform swimming," *J. Exp. Biol.*, vol. 213, pp. 2038–2047, 2010.

[41] K. Shoele and Q. Zhu, "Leading edge strengthening and the propulsion performance of flexible ray fins," *J. Fluid Mech.*, vol. 693, pp. 402–432, 2012.

[42] K. Shoele and Q. Zhu, "Performance of a wing with nonuniform flexibility in hovering flight," *Phys. Fluids*, vol. 25, no. 4, 2013.

[43] Qiang Zhu and Xiaobo Bi, "Effects of stiffness distribution and spanwise deformation on the dynamics of a ray-supported caudal fin," *Bioinspir. Biomim.*, vol. 12, no. 2, p. 26011, 2017.

[44] Q. Xiao and W. Liao, "Numerical investigation of angle of attack profile on propulsion performance of an oscillating foil," *Comput. Fluids*, vol. 39, no. 8, pp. 1366–1380, 2010.

[45] Q. Xiao, W. Liao, S. Yang, and Y. Peng, "How motion trajectory affects energy extraction performance of a biomimic energy generator with an oscillating foil?," *Renew. Energy*, vol. 37, no. 1, pp. 61–75, 2012.

[46] W. Liu, Q. Xiao, and F. Cheng, "A bio-inspired study on tidal energy extraction with flexible flapping wings," *Bioinspir. Biomim*, vol. 8, no. 3, pp. 36011–16, 2013.

[47] W. Liu, Q. Xiao, and Q. Zhu, "Passive Flexibility Effect on Oscillating Foil Energy Harvester," *AIAA J.*, vol. 54, no. 4, pp. 1172–1187, 2016.

[48] G. Shi, Q. Xiao, and Q. Zhu, "A Study of 3D Flexible Caudal Fin for Fish Propulsion," in *Proceedings of the 36th International Conference on Offshore Mechanics and Arctic Engineering*, 2017, no. OMAE2017-61528.

[49] W. Liao, J. Cai, and H. M. Tsai, "A multigrid overset grid flow solver with implicit hole cutting method," *Comput. Methods Appl. Mech. Eng.*, vol. 196, no. 9–12, pp. 1701–1715, 2007.

[50] A. Jameson, W. Schmidt, and E. L. I. Turkel, "Numerical solution of the Euler equations by finite volume methods using Runge Kutta time stepping schemes," in *14th Fluid and Plasma Dynamics Conference*, American Institute of Aeronautics and Astronautics, 1981.

[51] A. Jameson, "Time Dependent Calculations Using Multigrid, with Applications to Unsteady Flows Past Airfoils and Wings," *AIAA 10th Computational Fluid Dynamics Conference*. p. 14, 1991.

[52] M. Sadeghi, "Parallel Computation of Three Dimensional Aeroelastic Fluid-Structure Interaction," PhD Thesis, University of California, Irvine, 2004.

[53] B. S. H. CONNELL and D. K. P. YUE, "Flapping dynamics of a flag in a uniform stream," *J. Fluid Mech.*, vol. 581, pp. 33–67, 2007.

[54] Y. Lee and J. Baeder, "Implicit Hole Cutting - A New Approach to Overset Grid Connectivity," in *16th AIAA Computational Fluid Dynamics Conference*, American Institute of Aeronautics and Astronautics, 2003.

[55] H. M. Tsai, A. S. F. Wong, J. Cai, Y. Zhu, and F. Liu, "Unsteady Flow Calculations with a Parallel Multiblock Moving Mesh Algorithm," *AIAA J.*, vol. 39, no. 6, pp. 1021–1029, 2001.

[56] J. T. Batina, "Unsteady Euler algorithm with unstructured dynamic mesh for complex-aircraft aerodynamic analysis," *AIAA J.*, vol. 29, no. 3, pp. 327–333, 1991.

[57] U. Küttler and W. A. Wall, "Fixed-point fluid-structure interaction solvers with dynamic relaxation," *Comput. Mech.*, vol. 43, no. 1, pp. 61–72, 2008.

[58] C. Wood, A. J. Gil, O. Hassan, and J. Bonet, "Partitioned block-Gauss-Seidel coupling for dynamic fluid-structure interaction," *Comput. Struct.*, vol. 88, no. 23–24, pp. 1367–1382, 2010.

[59] C. Farhat and M. Lesoinne, "Two efficient staggered algorithms for the serial and parallel solution of three-dimensional nonlinear transient aeroelastic problems," *Comput. Methods Appl. Mech. Eng.*, vol. 182, no. 3–4, pp. 499–515, 2000.

26

[60] G. S. L. Goura, K. J. Badcock, M. A. Woodgate, and B. E. Richards, "A data exchange method for fluid-structure interaction problems," *Aeronaut. J.*, vol. 105, no. 1046, pp. 215–221, Apr. 2001.

[61] M. Sadeghi, F. Liu, K. L. Lai, and H. M. Tsai, "Application of Three-Dimensional Interfaces for Data Transfer in Aeroelastic Computations," in *22nd Applied Aerodynamics Conference and Exhibit*, American Institute of Aeronautics and Astronautics, 2004, pp. 1–30.

[62] B. N. Rajani, A. Kandasamy, and S. Majumdar, "Numerical simulation of laminar flow past a circular cylinder," *Appl. Math. Model.*, vol. 33, no. 3, pp. 1228–1247, 2009.

[63] E. Constant, J. Favier, M. Meldi, P. Meliga, and E. Serre, "An immersed boundary method in OpenFOAM : Verification and validation," *Comput. Fluids*, vol. 157, pp. 55–72, 2017.

[64] C. Kassiotis, A. Ibrahimbegovic, R. Niekamp, and H. G. Matthies, "Nonlinear fluid-structure interaction problem. Part I: Implicit partitioned algorithm, nonlinear stability proof and validation examples," *Comput. Mech.*, vol. 47, no. 3, pp. 305–323, 2011.

[65] C. Habchi *et al.*, "Partitioned solver for strongly coupled fluid-structure interaction," *Comput. Fluids*, vol. 71, pp. 306–319, 2013.

[66] H. G. Matthies and J. Steindorf, "Partitioned strong coupling algorithms for fluid–structure interaction," *Comput. Struct.*, vol. 81, no. 8–11, pp. 805–812, May 2003.

[67] H. Dong, R. Mittal, M. Bozkurttas, and F. Najjar, "Wake Structure and Performance of Finite Aspect-Ratio Flapping Foils," *43rd AIAA Aerosp. Sci. Meet. Exhib.*, no. January, pp. 1–9, 2005.
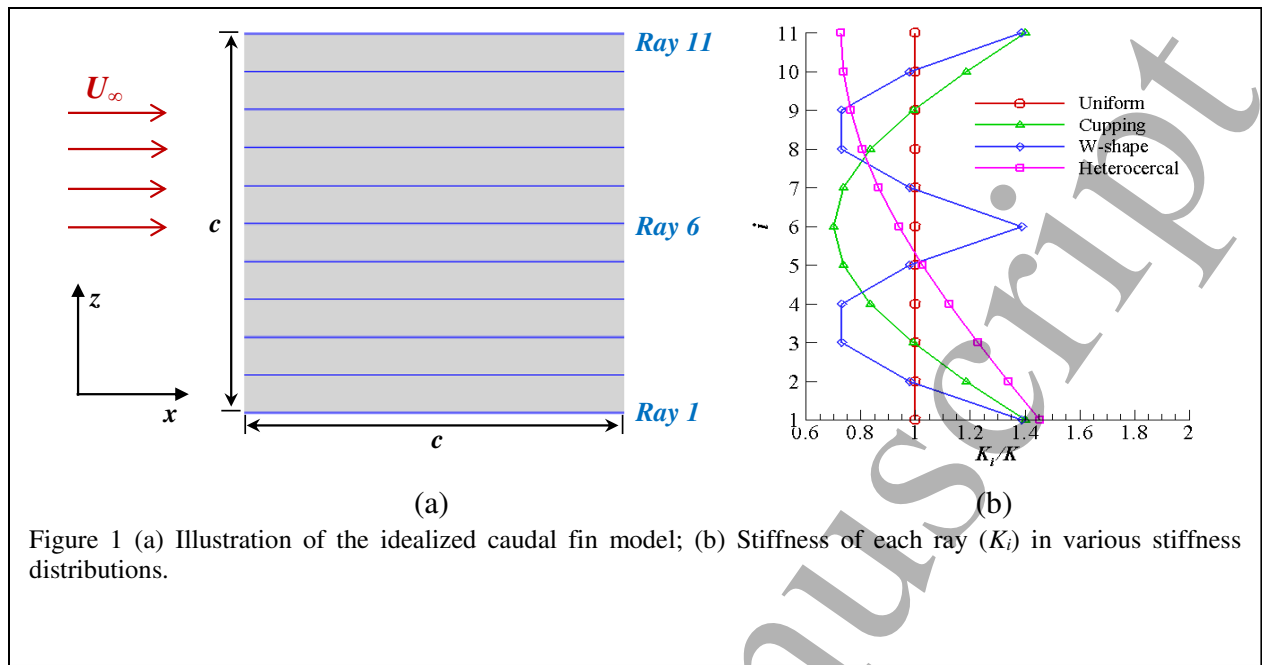
Figure 1 (a) Illustration of the idealized caudal fin model; (b) Stiffness of each ray (K_i) in various stiffness distributions.
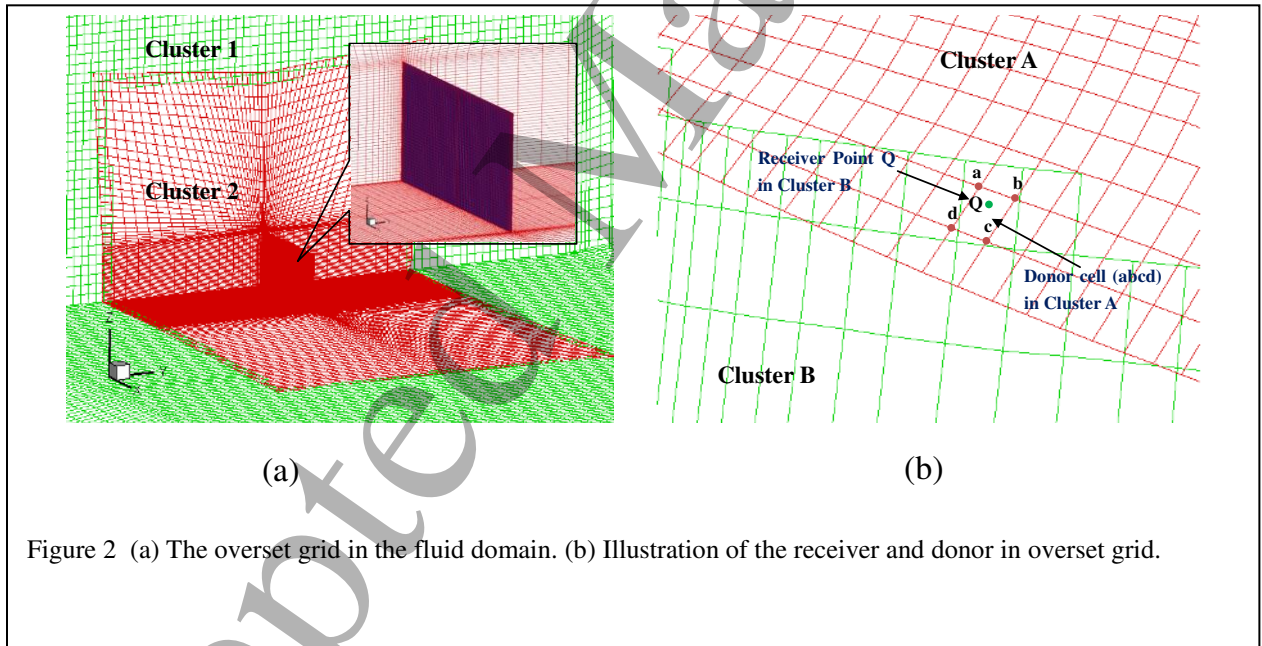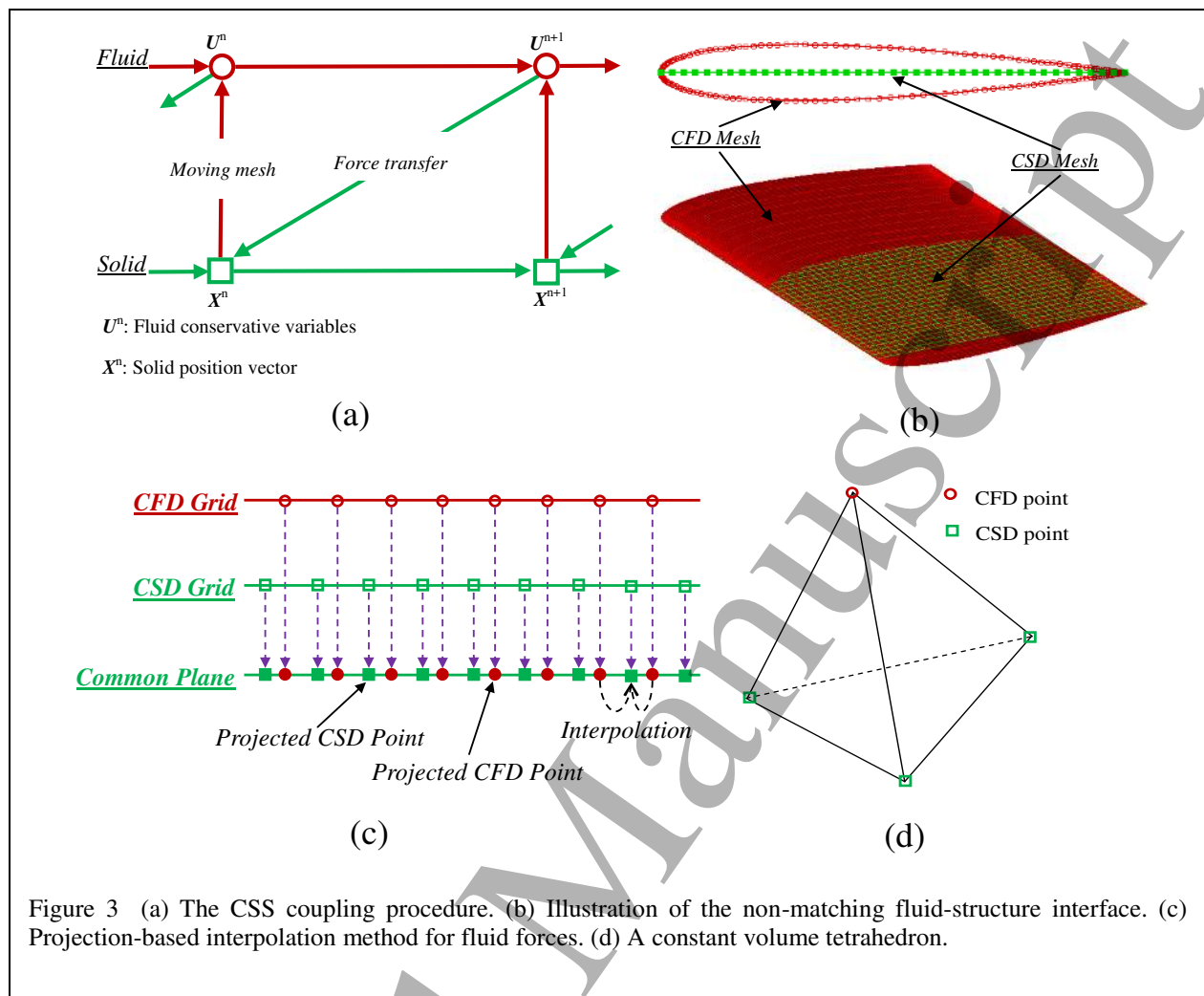

Figure 2 (a) The overset grid in the fluid domain. (b) Illustration of the receiver and donor in overset grid.

28

Figure 3   (a) The CSS coupling procedure. (b) Illustration of the non-matching fluid-structure interface. (c) Projection-based interpolation method for fluid forces. (d) A constant volume tetrahedron.
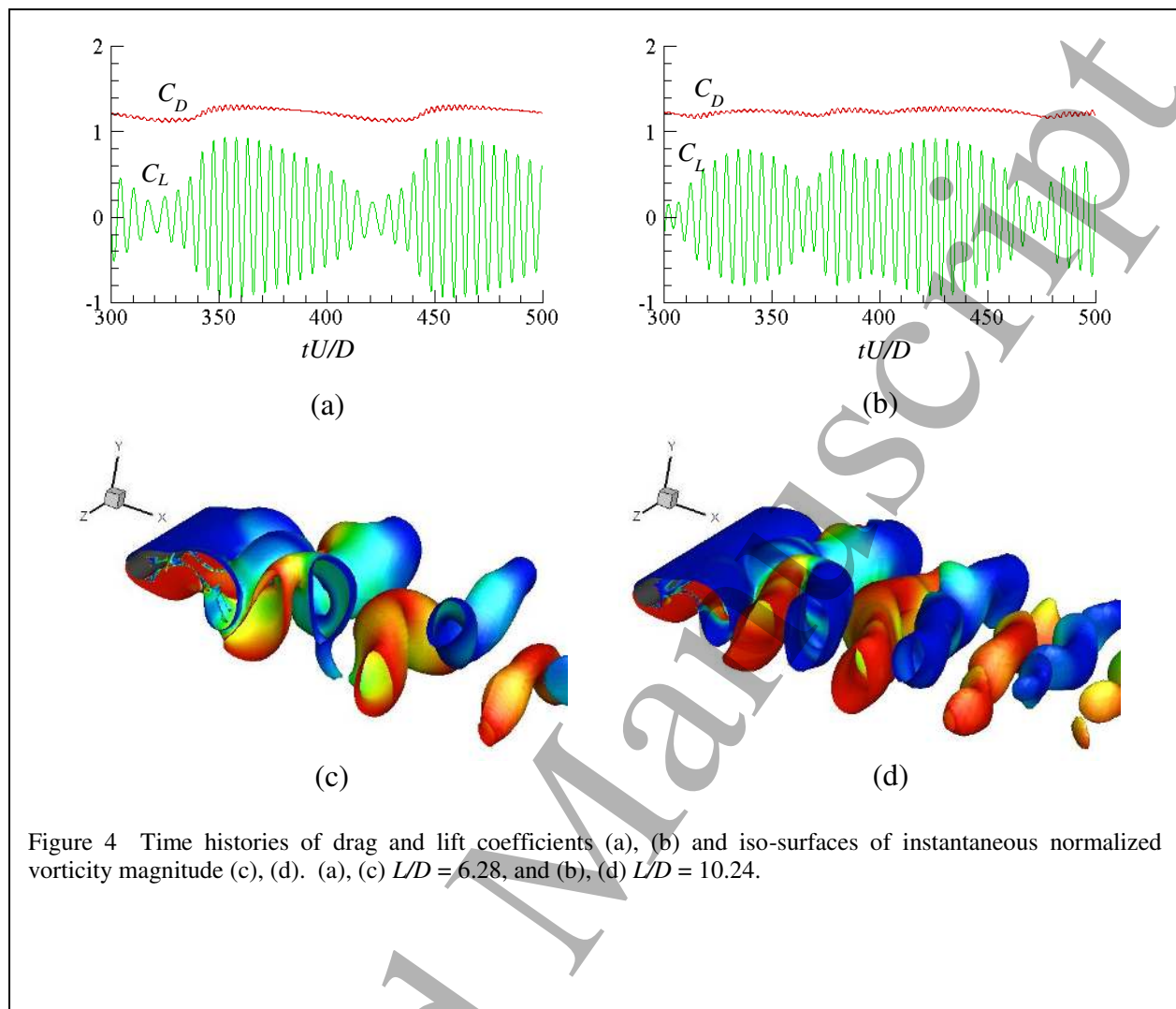
Figure 4   Time histories of drag and lift coefficients (a), (b) and iso-surfaces of instantaneous normalized vorticity magnitude (c), (d). (a), (c) L/D = 6.28, and (b), (d) L/D = 10.24.

Table 1 Mean drag and r.m.s. lift coefficients for flow past a stationary 3D cylinder at Re = 300. Numerical data from the literature is provided for comparison.

	L/D	$C_{d,mean}$	$C_{l,rms}$
Present	6.28	1.217	0.463
Present	10.24	1.234	0.466
Rajani et al. [62]	6.28	1.284	0.525
Constant et al. [63]	10.24	1.430	0.453

Figure 5 First and second order bending modes of a cantilever from the present simulation and theory.
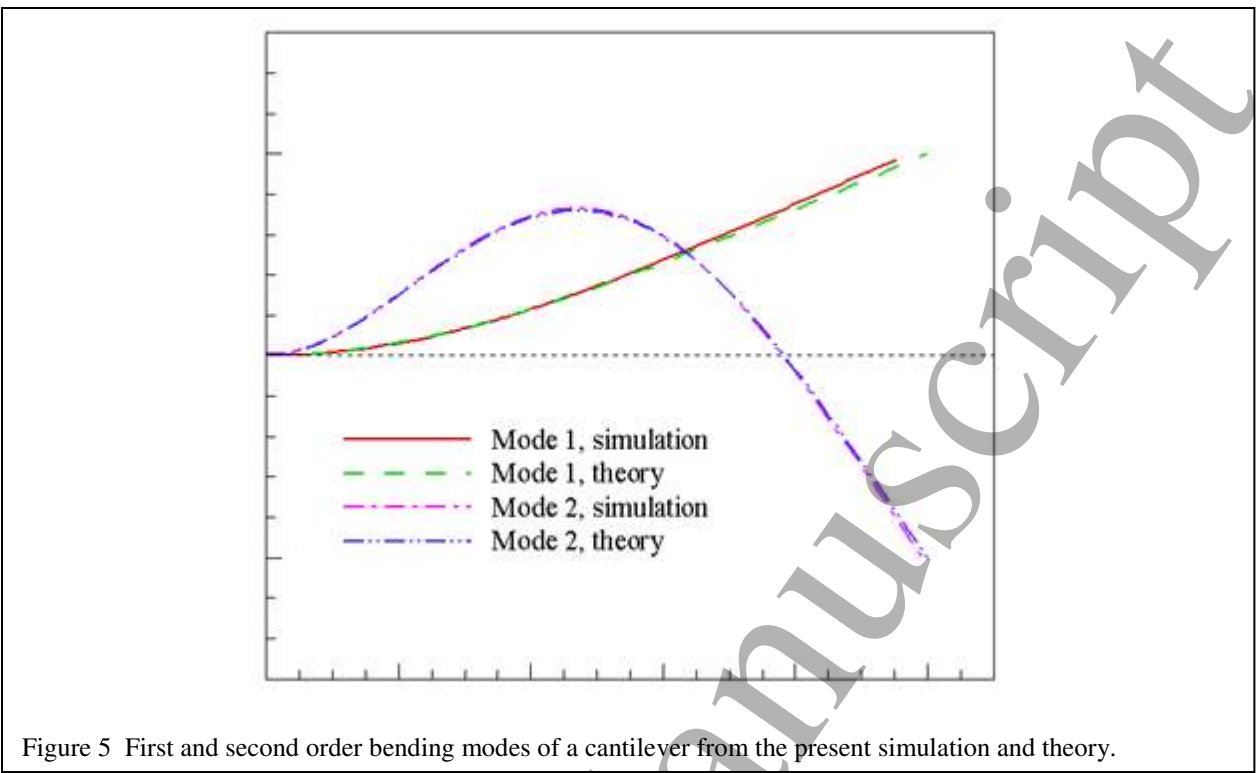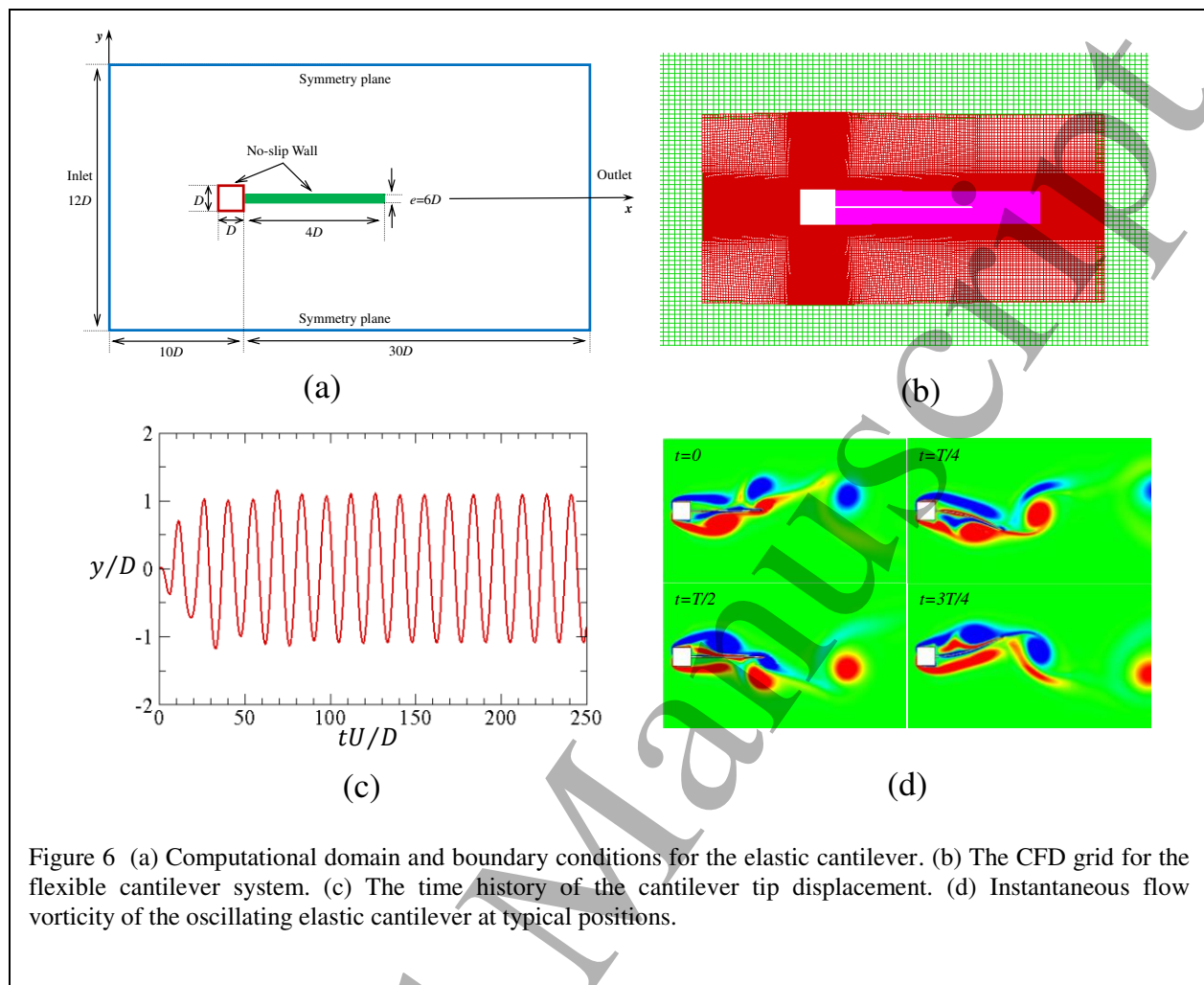
Figure 6　(a) Computational domain and boundary conditions for the elastic cantilever. (b) The CFD grid for the flexible cantilever system. (c) The time history of the cantilever tip displacement. (d) Instantaneous flow vorticity of the oscillating elastic cantilever at typical positions.

Table 2 Comparison of present result with those from open literature

Author	f_r	d_{max}^*
Matthies et al., 2003	0.192	1.18
Dettmer et al., 2006	0.185	1.25
Wood et al., 2010	0.179	1.15
Kassiotis et al., 2011	0.182	1.05
Habchi et al., 2013	0.201	1.02
Present study	0.211	1.12

Figure 7 Sensitivity study of the present code to (a) mesh density, (b) physical time step. Cupping distribution, K_B=1.0, S_t=0.4.
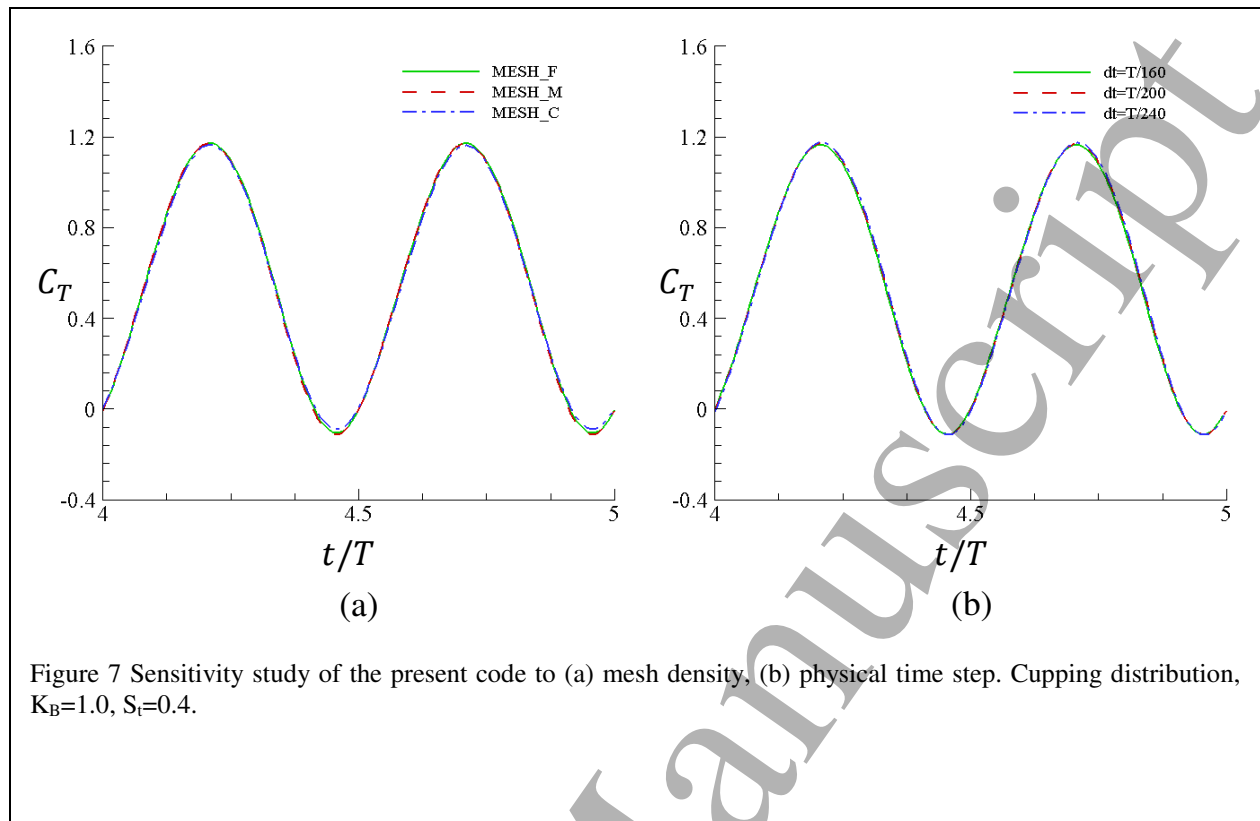
Table 3 CFD mesh and time-step sensitivity test results

	$\overline{C_T}$	$\overline{C_P}$	η
MESH_C, dt=T/200	0.545	2.980	0.183
MESH_F, dt=T/200	0.548	3.023	0.181
MESH_M, dt=T/200	0.547	3.024	0.180
MESH_M, dt=T/160	0.541	3.026	0.179
MESH_M, dt=T/240	0.545	3.023	0.180

Figure 8 Sketch of the computational domain for 3D caudal fin simulation.

Figure 9 Typical fin deformations for different ray stiffness distributions viewed from the top (left column) and behind (right column); (a) (b) uniform distribution; (c) (d) cupping distribution; (e) (f) W-shape distribution; (g) (h) heterocercal distribution.

Figure 10 Mean thrust coefficient $\overline{C_T}$, mean power expenditure coefficient $\overline{C_P}$ and propulsion efficiency η as functions of the mean bending stiffness K_b for different fin deformations at St=0.4.

Figure 11 Mean thrust coefficient $\overline{C_T}$, mean power expenditure coefficient $\overline{C_P}$ and propulsion efficiency η as functions of the mean bending stiffness K_b for different fin deformations at St=0.3.

37

Figure 12 Time histories of the instantaneous thrust coefficient C_T, lateral force coefficient C_Y and power expenditure coefficient C_P over one motion period for a rigid fin and a flexible fin (cupping distribution, K_b=0.5) at St=0.4.

Figure 13 Normalized displacements of leading edge y_L/c (red dash line), trailing edge y_T/c (blue dash-dot line) and effective pitch motion $(y_T - y_L)/c$ (green dash-dot-dot line) of Ray 6, and thrust coefficient C_T (pink solid line) in cupping distribution at St=0.4; (a) K_b=1.0, and (b) K_b=0.3.

Figure 14 Deflections in *y*-direction of Ray 1 (blue solid lines) and Ray 6 (red dash-dot lines) for (a) uniform distribution and (b) cupping distribution, *St*=0.4, K_b=0.5.

Figure 15 Iso-surfaces of vorticity magnitude in the wake behind a fin with different stiffness distributions; (a) uniform distribution, (b) cupping distribution, (c) w-shape distribution, and (d) heterocercal distribution. St=0.4, K_b=0.5, t=T/4.

Figure 16 Vorticity fields behind the flexible fin with (a) uniform, (b) cupping, (c) w-shape and (d) heterocercal ray stiffness distributions. The contours display the y-component of the vorticity within y=0 plane. St=0.4, K_b=0.5, t=T/4.